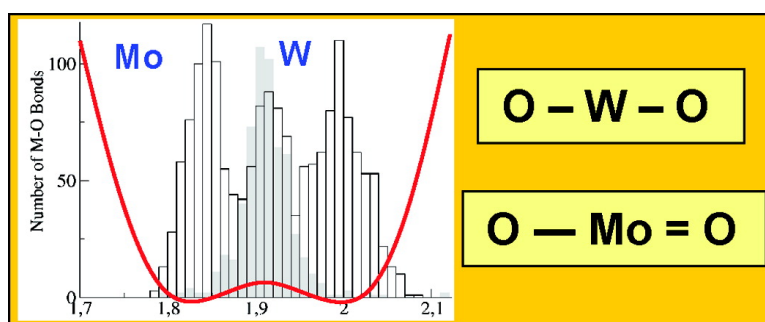Article

On the Origin of Alternating Bond Distortions and the Emergence of Chirality in Polyoxometalate Anions

Likai Yan, Xavier Lo#pez, Jorge J. Carbo#, Richard Sniatynsky, Dean C. Duncan, and Josep M. Poblet

More About This Article

Additional resources and features associated with this article are available within the HTML version:

- Supporting Information
- Links to the 2 articles that cite this article, as of the time of this article download
- Access to high resolution figures
- Links to articles and content related to this article
- Copyright permission to reproduce figures and/or text from this article

View the Full Text HTML

On the Origin of Alternating Bond Distortions and the Emergence of Chirality in Polyoxometalate Anions

Likai Yan,[‡] Xavier López,[*,†] Jorge J. Carbó,[†] Richard Sniatynsky,[§]
Dean C. Duncan,[*,§] and Josep M. Poblet[*,†]

*Departament de Química Física i Inorgànica, Universitat Rovira i Virgili, Marcel-lí Domingo
s/n, 43007 Tarragona, Spain, Institute of Functional Material Chemistry, Department of
Chemistry, Northeast Normal University, Changchun 130024, People's Republic of China, and
Department of Chemistry and Biochemistry, University of Wisconsin-Milwaukee,
Milwaukee, WI 53211-3029*

Received December 11, 2007; E-mail: josepmaria.poblet@urv.cat; javier.lopez@urv.cat; dcduncan@uwm.edu

Abstract: Alternating short and long bond length (ABL) distortions observed within the ring structures of molecular metal oxide anions or polyoxometalates (POMs) are reminiscent of the cooperative linear ABL distortions in perovskite d^0 metal oxides. We show herein that these distortions have a common origin: a pseudo Jahn–Teller (PJT) vibronic instability. Four POM structural types with different M_nO_n ring sizes are investigated herein using density functional theoretical methods: Lindqvist $[M_6O_{19}]^{q-}$ ($n = 4$), Keggin α-$[XM_{12}O_{40}]^{q-}$ ($n = 6$), Wells–Dawson α-$[X_2M_{18}O_{62}]^{q-}$ ($n = 8$), and Preyssler $[(Na)P_5W_{30}O_{110}]^{14-}$ ($n = 10$), where $M = Mo^{VI}$ and W^{VI} and $X = Si^{IV}$, Ge^{IV}, P^V, As^V, S^{VI}, and Se^{VI}. Chirality is induced within the latter three structural types by the ABL ring distortions. The calculations confirm the PJT vibronic origin of the ABL distortions with good agreement between calculated geometries and published single-crystal X-ray diffraction data. Both theory and experiment show that the vibronic interaction and distortion magnitude increase for (1) molybdates relative to that of tungstates, (2) larger M_nO_n ring sizes, (3) increases in negative charge of the internalized fragments (O^{2-} or XO_4^{q-}), and (4) d^0 versus d^n metal oxidation states. The PJT vibronic coupling model explains these observations in terms of the energy gap between Kohn–Sham frontier molecular orbitals (MOs) concomitant with the propensity for metal–oxygen π-bonding within the M_nO_n rings. The frontier MOs for the undistorted nuclear configurations are largely nonbonding π-O_p (occupied) and π-M_d (unoccupied) in character, where smaller HOMO–LUMO (H–L) gap energies lead to greater metal–oxygen π-orbital mixing under the influence of the nuclear distortion. A reduction in π-bond order decreases the distortion in mixed-valence POMs. Of the tungstates examined, only the Preyssler anion shows pronounced ABL ring distortions, which derive from its large ring size and concomitant small H–L gap.

Introduction

Both simple and complex metal oxides exhibit high structural variability that allows for cooperative symmetry-breaking interactions toward organized structures with intriguing and technologically important electronic, magnetic, dielectric, optical, and catalytic properties, including superconductivity, ferroelectricity, and colossal magnetoresistance, among others.[1–5] Some of these properties are related to cooperative off-center

displacements of the metal atoms from nominally high symmetry nuclear configurations. For metal oxides in nondegenerate ground states, such displacements originate from a pseudo Jahn–Teller vibronic instability.[5] For example, a typical metal oxide exhibiting such behavior is the perovskite ceramic $BaTiO_3$ in which the TiO_6 octahedra of the cubic phase distort in the same direction on forming the tetragonal phase by collective off-center displacements of the Ti atoms toward O atom vertices. These cooperative vibronic distortions form well-aligned linear chains of alternating short and long Ti–O bond lengths that

[‡] Northeast Normal University.
[†] Universitat Rovira i Virgili.
[§] University of Wisconsin-Milwaukee.
(1) (a) Fierro, J. L. G. *Metal Oxides: Chemistry and Applications*; CRC Taylor & Francis: Boca Raton, FL, 2005. (b) Rao, C. N. R.; Raveau, B. *Transition Metal Oxides*; Wiley & Sons: New York, 1998.
(2) *High Tc Superconductors and Related Transition-Metal Oxides: Special Contributions in Honor of K. Alex Müller on the Occasion of His 80th Birthday*; Bussmann-Holder, A., Keller, H., Eds.; Springer-Verlag: Berlin, 2007.
(3) Lines, M. E.; Glass, A. M. *Principles and Applications of Ferroelectrics and Related Materials*; Clarendon Press: Oxford, 1977.
(4) (a) *Colossal Magnetoresistive Oxides*; Tokura, Y., Ed.; Overseas Publishers Association: Amsterdam, 2000. (b) *Colossal Magnetoresistive Manganites*; Chatterji, T., Ed.; Kluwer Academic Publishers: Dordrecht, The Netherlands, 2004.

(5) (a) Englman, R. *The Jahn–Teller Effect in Molecules and Crystals*; Wiley-Interscience: London, 1972. (b) *Conical Intersections: Electronic Structure, Dynamics, and Spectroscopy*; Domcke, W., Yarkony, D. R., Köppel, H., Eds.; World Scientific: Singapore, 2004. (c) Bersuker, I. *The Jahn Teller Effect*; Cambridge University Press: Cambridge; 2006. (d) Chapter 8 of ref[5c] contains an excellent discussion with numerous references on cooperative vibronic phenomena. (e) The PJT interaction is referred to by some as a second-order JT interaction, but this nomenclature is misleading, as pointed out in ref,[5c] p 111. The more descriptive term, "orbital ordering", also has been used to describe the cooperative PJT interaction in certain correlated d^n systems such as charge-ordered "stripe phases" in manganites. For example, see: Tokunaga, Y.; Lottermoser, T.; Lee, Y.; Kumai, R.; Uchida, M.; Arima, T.; Tokura, Y. *Nature* **2006**, *5*, 937.

lead to charge polarization and the emergence of strong ferroelectric behavior in the tetragonal phase of the crystal.[3,6] Alternating short and long bond length (ABL) distortions that are driven by vibronic instabilities at symmetric configurations are observed in many other systems in addition to metal oxides, including 1-D conjugated polymers,[7–9] metal-coordination polymers,[8–10] and other inorganic[11] and organic systems.[12]

Similar concerted short and long bond length alternations are observed within metal oxide ring structures, M_nO_n, of certain molecular metal oxide anions or polyoxometalates (POMs),[13] but the origin of these distortions has not been explained satisfactorily. These polycyclic high valent metal oxides of groups 5 and 6 metals (chromium excluded) are structurally diverse with metal coordination numbers ranging from 4 to 7 that derive from a balance between the polarizing ability and charge capacity of these metals within oxide coordination spheres. However, the structures typically are built from pseudo-octahedral MO_6 units that, in the absence of ring distortions, approximate C_{4v} local symmetry featuring metal–oxygen bonds to four equatorial bridging oxygens with the metal displaced out of the equatorial plane toward the anion periphery.[13] This produces a short bond to the terminal surface oxygen and a long bond to the internalized bridging oxygen (either O^{2-} or XO_4^{q-}) situated trans to the terminal oxo ligand. Closed oligomeric frameworks are created by the fusion of these units at edges, corners, and/or faces via both the bridging equatorial and internalized oxygen atom vertices forming interpenetrating metal oxide rings, M_nO_n, of various sizes. For rings that exhibit ABL distortions, the local symmetry of associated MO_6 octahedra changes from C_{4v} to C_s. Examination of ABL ring distortions within the following four typical POM structures (Figure 1) is considered herein: (1) the Lindqvist structure, $[M_6O_{19}]^{q-}$ (M_6)[14] of nominal O_h symmetry constructed from three interpenetrating rings ($n = 4$), (2) the α-Keggin structure, α-$[XM_{12}O_{40}]^{q-}$ (XM_{12}) of nominal T_d symmetry with four rings ($n = 6$), (3) the α-Wells−Dawson structure, α-$[X_2M_{18}O_{62}]^{q-}$ (X_2M_{18}) of nominal D_{3h} symmetry with three rings aligned along the principal axis ($n = 8$) and two rings perpendicular to this axis ($n = 6$), and (4) the Pope−Jeannin−Preyssler anion, $[(Na)P_5W_{30}O_{110}]^{14-}$ (P_5W_{30}) of nominal D_{5h} symmetry with two rings ($n = 10$).

The first clear evidence for ABL distortions in these POM ring structures was obtained from single-crystal X-ray investigations conducted by several groups in the mid-1970s. Allcock and co-workers identified significant Mo_4O_4 ring distortions in a cyclophosphazene salt of $[Mo_6O_{19}]^{2-}$ (Mo_6).[15] This result was confirmed for other hexamolybdate salts with different counterions,[16a–g] although a significant number of Mo_6 structures also appeared with little[16h,i] or no distortion.[16j,k] The first ABL distortions were identified in a Keggin derivative, α-$[PMo_{12}O_{40}]^{3-}$ (PMo_{12}),[17a–c] which was observed later in α-$[GeMo_{12}O_{40}]^{4-}$ ($GeMo_{12}$)[17d] and α-$[SiMo_{12}O_{40}]^{4-}$ ($SiMo_{12}$).[17e] Both Strandberg and D'Amour also reported ABL distortions within the three Mo_8O_8 rings of α-$[P_2Mo_{18}O_{62}]^{6-}$ (P_2Mo_{18}),[18] and Hori and co-workers observed similar but somewhat smaller distortions in α-$[S_2Mo_{18}O_{62}]^{4-}$ (S_2Mo_{18}).[19] In contrast to the molybdates, crystal structures of the Lindqvist,[20] Keggin,[21] and Wells−Dawson[18a,22] *tungstates* either fail to show significant ring distortions within the uncertainties of measurement or are greatly diminished relative

(6) (a) Bersuker, I. B. *Phys. Lett.* **1966**, *20*, 586. (b) Bersuker, I. B. *Ferroelectrics* **1995**, *164*, 75. (c) Ghosez, P.; Cockayne, E.; Waghmare, U. V.; Rabe, K. M. *Phys. Rev.* **1999**, *B90*, 836. (d) Chen, Z.; Chen, Y.; Jiang, Y. *J. Phys. Chem. B* **2001**, *105*, 5766, and references therein.

(7) Barford, W. *Electronic and Optical Properties of Conjugated Polymers*; Clarendon Press: Oxford, 2005 and references therein.

(8) Roth, S.; Carroll, D. *One-Dimensional Metals*; Wiley-VCH: Weinheim, Germany, 2004 and references therein.

(9) Peierls, R. E. *Quantum Theory of Solids*; Oxford University Press: London, 1955.

(10) (a) Wheeler, R. A.; Whangbo, M.; Hughbanks, T.; Hoffman, R.; Burdett, J.; Albright, T. *J. Am. Chem. Soc.* **1986**, *108*, 2222. (b) Wheeler, R. A.; Hoffmann, R.; Strähle, J. *J. Am. Chem. Soc.* **1986**, *108*, 5381.

(11) (a) Strähle, J. *Z. Anorg. Allg. Chem.* **1970**, *375*, 238. (b) Strähle, J. *Z. Anorg. Allg. Chem.* **1971**, *380*, 96. (c) Musterle, W.; Strähle, J.; Liebelt, W.; Dehnicke, K. *Z. Naturforsch.* **1979**, *B35*, 942. (d) Walker, I.; Strähle, J.; Ruschke, P.; Dehnicke, K. *Z. Anorg. Allg. Chem.* **1982**, *487*, 26. (e) Müller, U.; Kujanek, R.; Dehnicke, K. *Z. Anorg. Allg. Chem.* **1982**, *495*, 127. (f) Figge, R.; Friebel, C.; Patt-Siebel, U.; Müller, U.; Dehnicke, K. *Z. Naturforsch.* **1989**, *44b*, 1377. (g) Herrmann, W. A.; Bogdanovic, S.; Behm, J.; Denk, M. *J. Organomet. Chem.* **1992**, *C33*, 430. (h) Ergezinger, C.; El-Kholi, A.; Müller, U.; Dehnicke, K. *Z. Anorg. Allg. Chem.* **1989**, *568*, 55. (i) Görge, A.; Patt-Siebel, U.; Müller, U.; Dehnicke, K. *Z. Naturforsch.* **1989**, *44b*, 903. (j) Sarasa, J. P.; Poblet, J. M.; Bénard, M. *Organometallics* **2000**, *19*, 2264.

(12) (a) Berry, R. S. *J. Chem. Phys.* **1961**, *35*, 2253. (b) Haas, Y.; Zilberg, S. *J. Am. Chem. Soc.* **1995**, *117*, 5387. (c) Heilbronner, E. *J. Chem. Educ.* **1989**, *66*, 471. (d) Stanger, A.; Vollhardt, K. P. C. *J. Org. Chem.* **1988**, *53*, 4889. (e) Epiotis, N. D. *Pure Appl. Chem.* **1983**, *55*, 229. (f) Yang, S.; Kertesz, M. *J. Phys. Chem. A* **2006**, *110*, 9771. (g) Venkatesan, T. S.; Mahapatra, S.; Meyer, H.-D.; Köppel, H.; Cederbaum, L. S. *J. Phys. Chem. A* **2007**, *111*, 1746. (h) Koseki, S.; Toyota, A. *J. Phys. Chem. A* **1997**, *101*, 5712. (i) Barlow, S.; Henling, L. M.; Day, M. W.; Schaefer, W. P.; Green, J. C.; Hascall, T.; Marder, S. R. *J. Am. Chem. Soc.* **2002**, *124*, 6285. (j) Jacquemin, D.; Femenias, A.; Chermette, H.; Ciofini, I.; Adamo, C.; André, J.-M.; Perpète, E. A. *J. Phys. Chem. A* **2006**, *110*, 5952. (k) Zhao, Y.; Truhlar, D. G. *J. Phys. Chem. A* **2006**, *110*, 10478. (l) Pierrefixe, S. C. A. H.; Bickelhaupt, F. M. *Chem.−Eur. J.* **2007**, *13*, 6321.

(13) (a) Pope, M. T. *Heteropoly and Isopoly Oxometalates*; Springer-Verlag: Berlin, 1983. (b) *Polyoxometalate Molecular Science*; Borrás-Almenar, J. J., Coronado, E., Müller, A., Pope, M. T., Eds.; Kluwer Academic Publishers: Dordrecht, The Netherlands, 2003. (c) Pope, M. T. *Polyoxo Anions: Synthesis and Structure*. In *Comprehensive Coordination Chemistry II: From Biology to Nanotechnology*; Wedd, A. G., Ed.; Elsevier: New York, 2004; Vol. 4, pp 635−678.

(14) After completely specifying an anion formula, $[X_nM_oO_p]^{q-}$, we will use the following short-hand notation, X_nM_o, throughout.

(15) (a) Allcock, H. R.; Bissell, E. C.; Shawl, E. T *J. Am. Chem. Soc.* **1972**, *94*, 8603. (b) Allcock, H. R.; Bissell, E. C.; Shawl, E. T. *Inorg. Chem.* **1973**, *12*, 2963.

(16) (a) Ghammani, S. *Cryst. Res. Technol.* **2003**, *38*, 913. (b) Boyle, P. D.; Stauffer, T. C.; Wirgau, J. I.; Cornman, C. R. *Acta Crystallogr.* **1998**, *C54*, IUC9800011. (c) Coronado, E.; Galan-Mascaros, J. R.; Gimenez-Saiz, C.; Gomez-Garcia, C. J.; Rovira, C.; Tarres, J.; Triki, S.; Veciana, J. *J. Mater. Chem.* **1998**, *8*, 313. (d) Triki, S.; Ouahab, L.; Grandjean, D.; Fabre, J. M. *Acta Crystallogr.* **1991**, *C47*, 645. (e) Long, D.-L.; Kögerler, P.; Cronin, L. *Angew. Chem., Int. Ed.* **2004**, 1817. (f) Modec, B.; Brencic, J. V.; Zubieta, J. *J. Chem. Soc., Dalton Trans.* **2002**, 1500. (g) Garner, C. D.; Howlader, N. C.; Mabbs, F. E.; McPhail, A. T.; Miller, R. W.; Onan, K. D. *J. Chem. Soc., Dalton Trans.* **1978**, 1582. (h) Dahlstrom, P.; Zubieta, J.; Neaves, B.; Dilworth, J. R. *Cryst. Struct. Commun.* **1982**, *11*, 463. (i) Zhao, P. S.; Zhao, Z. R.; Jian, F. F.; Lu, L. D. *J. Korean Chem. Soc.* **2003**, *47*, 553. (j) Strukan, N.; Cincric, M.; Devcic, M.; Giester, G.; Kamenar, B. *Acta Crystallogr.* **2000**, *C56*, e278. (k) Wu, D.; Wang, S.; Lin, X.; Lu, C.; Zhuang, H. *Acta Crystallogr.* **2000**, *C56*, e55.

(17) (a) Strandberg, R. *Acta Chem. Scand., Ser. A* **1975**, *29*, 359. (b) D'Amour, H.; Allmann, R. *Z. Kristallogr.* **1976**, *143*, 1. (c) Neier, R.; Trojanowski, C.; Mattes, R. *J. Chem. Soc., Dalton Trans.* **1995**, *2521*, 2528. (d) Strandberg, R. *Acta Crystallogr.* **1977**, *B33*, 3090. (e) Ichida, H.; Kobayashi, A.; Sasaki, Y. *Acta Crystallogr.* **1980**, *B36*, 1382.

(18) (a) Strandberg, R. *Acta. Chem. Scand., Ser. A* **1975**, *29*, 350. (b) D'Amour, H. *Acta Crystallogr.* **1976**, *B32*, 729.

(19) Hori, T.; Tamada, O.; Himeno, S. *J. Chem. Soc., Dalton Trans.* **1989**, 1491.

(20) (a) Fuchs, J.; Freiwald, W.; Hartl, H. *Acta Crystallogr.* **1978**, *B34*, 1764. (b) Willing, W.; Muller, U.; Berg, A. *Acta Crystallogr.* **1986**, *C42*, 1644. (c) Triki, S.; Ouahab, L.; Padiou, J.; Grandjean, D. *Chem. Commun.* **1989**, 1968. (d) Yang, W.-B.; Lu, C.-Z.; Wu, C.-D.; Yu, Y.-Q.; Zhang, Q.-Z.; Chen, S.-M. *J. Cluster Sci.* **2003**, *14*, 421.
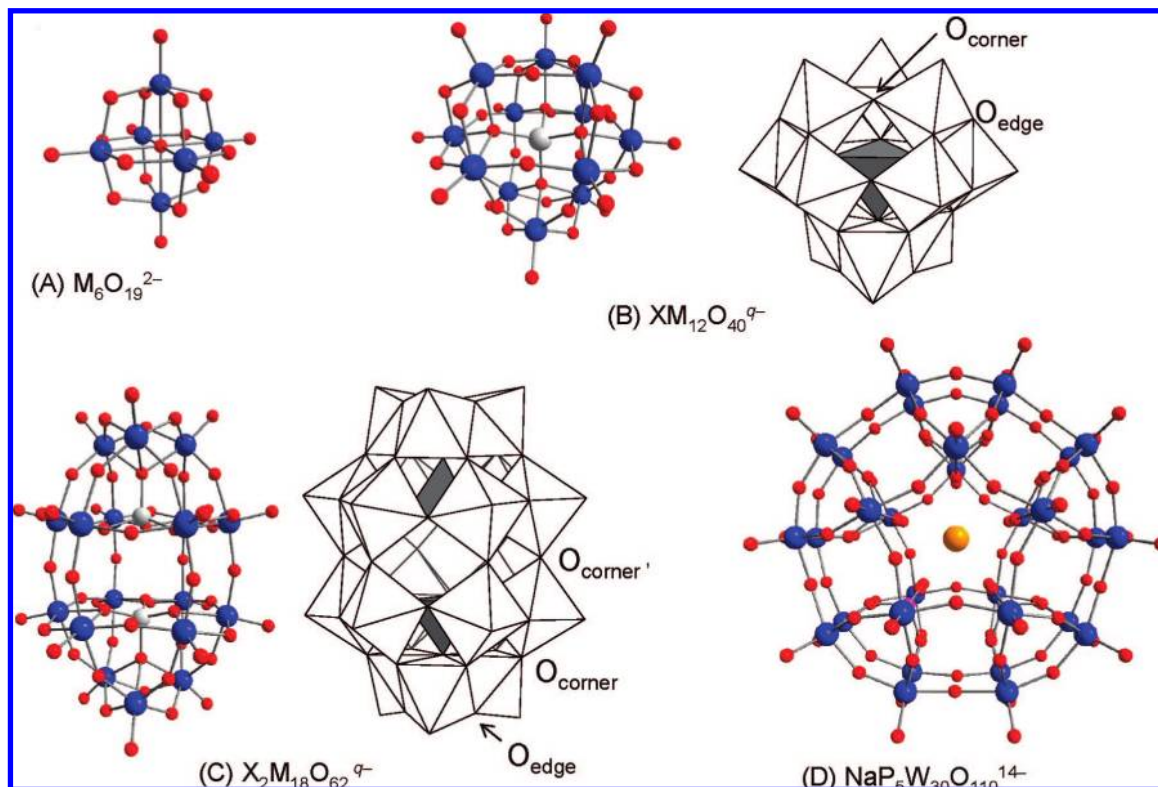
Figure 1. Ball-and-stick view of the following POM structures: (A) $[M_6O_{19}]^{2-}$, (B) α-$[XM_{12}O_{40}]^{q-}$, (C) α-$[X_2M_{18}O_{62}]^{q-}$, and (D) $[(Na)P_5W_{30}O_{110}]^{14-}$. Blue and red spheres represent metal (M = Mo, W) and oxygen atoms, respectively; white spheres represent heteroatoms X = P, As, Si, Ge, S. (D) The orange sphere represents the Na^+ cation. (B, C) Polyhedral representation including the types of bridging oxygens with the definition of the three types of bridging oxygens.

to the molybdates. However, Pope and co-workers did observe significant ABL distortions within the two $W_{10}O_{10}$ rings of P_5W_{30}.[23]

Examination of these early POM crystal structures clearly shows that the ABL distortions in the M_nO_n rings derive from metal atom off-center displacements[24] because the O···O distances remain relatively constant. Therefore, the oxide ligands in POMs are best viewed as fairly rigid close-packed structures as noted also by Garvey and Pope[25] and Klemperer et al.[26] The metal displacements change the anion symmetries, reducing the Lindqvist from O_h to either S_6 (all three rings distorted equally)[16a] or C_i,[16b–h] the Keggin from T_d to chiral T, the Wells–Dawson from D_{3h} to chiral D_3, and P_5W_{30} from D_{5h} to chiral D_5. Pope first recognized the induction of chirality in the latter three structures.[27] Moreover, Garvey and Pope showed that this chirality persists in solution for P_2Mo_{18} by observation of a Pfeiffer effect in its optical rotatory dispersion spectrum due to ion-pairing with chiral countercations.[25] Because the

Pfeiffer effect describes the formation of an enantiomeric excess starting from a racemic mixture, they concluded that the P_2Mo_{18} enantiomers must be interconverting in aprotic nonaqueous solutions. However, no detectable Pfeiffer effect was experimentally observed for $SiMo_{12}$ (chiral),[25] Mo_6 (achiral),[25] or S_2Mo_{18} (chiral),[19] all of which show smaller ABL ring distortions in their crystal structures relative to that of P_2Mo_{18}.

Aside from chirality, the significance of the metal oxide ABL ring distortions on redox, basicity, and other chemical properties of POMs has received little attention. However, Garvey and Pope[25] did propose that the "anomalous" redox behavior of P_2Mo_{18} in aqueous solution, namely two-electron reductions as opposed to separate one-electron steps,[28,29] could be related to a restructuring of the distorted anion to a more symmetrical configuration. In a related point, for the two-electron reduced mixed-valence complexes, $X_2Mo_{18}(2e^-)$, the observation of a diminished Pfeiffer effect (X = P)[25] and a significant reduction in Mo_8O_8 ABL ring distortions (X = S)[17c] relative to the fully oxidized anions indicates that ABL distortions decrease following POM reduction. Furthermore, the general trend that molybdates are more basic than tungstates[13] is reversed for P_2Mo_{18} and P_2W_{18},[30] which we suspect could also be related to the chiral distortion in P_2Mo_{18}.

A convincing explanation for the origin of the ABL distortions observed in POM crystal structures has not been brought

(21) (a) Keggin, J. F. *Nature* **1933**, *131*, 908. (b) Brown, G. M.; Noe-Spirlet, M. R.; Busing, W. R.; Levy, H. A. *Acta Crystallogr.* **1977**, *B33*, 1038. (c) Noe-Spirlet, M. R.; Brown, G. M.; Busing, W. R.; Levy, H. A. *Acta Crystallogr.* **1975**, *A31*, S80. (d) Fuchs, J.; Thiele, A.; Palm, R. *Z. Naturforsch.* **1981**, *36b*, 161.
(22) Dawson, B. *Acta Crystallogr.* **1953**, *6*, 113.
(23) (a) Alizadeh, M. H.; Harmalker, S. P.; Jeannin, Y.; Martin-Frère, J.; Pope, M. T. *J. Am. Chem. Soc.* **1985**, *107*, 2662. (b) Kim, K. C.; Pope, M. T.; Gama, G. J.; Dickman, M. H. *J. Am. Chem. Soc.* **1999**, *121*, 11164.
(24) Megaw, H. D. *Acta Crystallogr.* **1968**, *B24*, 149.
(25) Garvey, J. F.; Pope, M. T. *Inorg. Chem.* **1978**, *17*, 1115.
(26) (a) Besecker, C. J.; Day, V. W.; Klemperer, W. G.; Thompson, M. R. *J. Am. Chem. Soc.* **1984**, *106*, 4125. (b) Day, V. W.; Klemperer, W. G.; Maltbie, D. J. *J. Am. Chem. Soc.* **1987**, *109*, 2991.
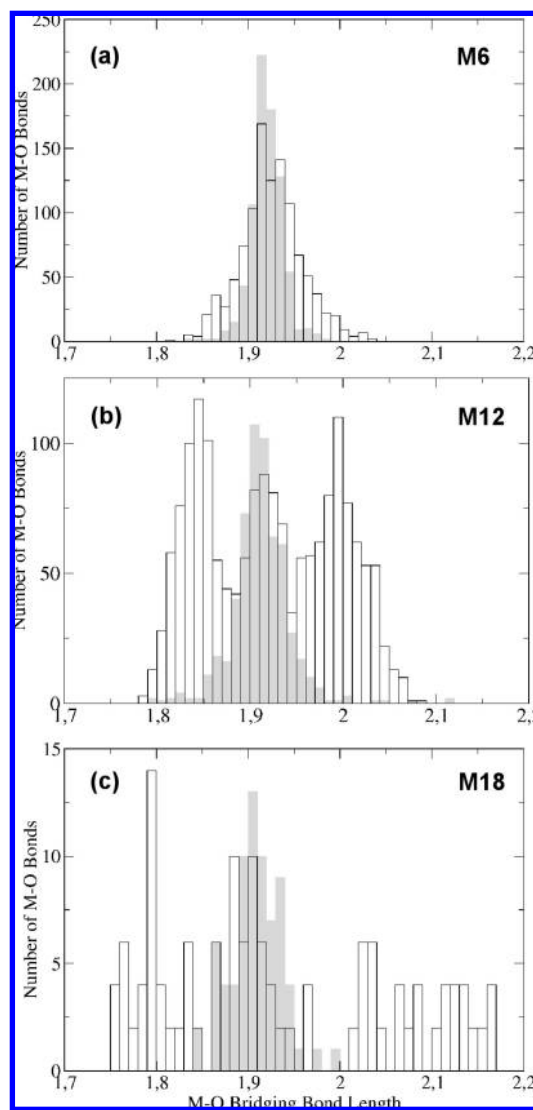(27) Pope, M. T. *Inorg. Chem.* **1976**, *15*, 2008.

(28) (a) Souchay, P.; Contant, R.; Fruchart, J. M. *C. R. Hebd. Seances Acad. Sci., Ser. C* **1967**, *264*, 976. (b) Contant, R.; Fruchart, J. M. *Rev. Chim. Miner.* **1974**, *11*, 123.
(29) (a) Papaconstantinou, E.; Pope, M. T. *Inorg. Chem.* **1967**, *6*, 1152. (b) Pope, M. T.; Papaconstantinou, E. *Inorg. Chem.* **1967**, *6*, 1147.
(30) Timofeeva, M. N. *Appl. Catal., A* **2003**, *256*, 19.

forward. In addition, the difference in tendency toward distortion between molybdates and tungstates, differences across various POM structures, and the emergence of smaller distortions on POM reduction to mixed-valence systems have not been explained satisfactorily. However, "crystal packing effects" have been invoked to explain the *variations* in ABL distortions apparent in different crystal structures of the same anion.[16,17e] Garvey and Pope argue that the persistence of chirality in solutions of P_2Mo_{18} indicates that some other influence must be responsible for these distortions, and they also point to the empirical observation that Mo centers in *most* molybdates have terminal *cis*-dioxo coordination whereas *most* tungstates prefer single terminal oxo coordination.[25] D'Amour also has suggested that the greater propensity for distortion in molybdates is linked to differences in the core–electron compressibilities between molybdenum and tungsten, as well as to differences in the radial extensions between the 4d and 5d orbitals.[18b]

The quantum chemistry group in Tarragona has been working toward a greater understanding of the structure, bonding, and properties of POMs.[31,32] From computational results using density functional theoretical (DFT) methods, we demonstrate that the Lindqvist, α-Keggin, α-Wells–Dawson, and Pope–Jeannin–Preyssler POM structures show a vibronic instability or near-instability at their highest symmetry nuclear configurations consistent with the pseudo Jahn–Teller (PJT) vibronic coupling formalism. This vibronic instability is the origin of the concerted ABL distortions and concomitant chiral induction observed in POM crystal structures. Our results show that the PJT vibronic interaction is particularly pronounced for the molybdates relative to the tungstates and increases with both the M_nO_n ring size and the negative charge of internalized fragments (O^{2-} or XO_4^{q-}), in excellent agreement with all available experimental data. We also confirm that ABL distortions diminish on POM reduction to mixed-valence states and that PJT vibronic interactions can exert substantial influence on POM reduction potentials.

Results and Discussion

Comparison of Experimental and Calculated Lindqvist, Keggin, and Wells–Dawson Structures. To quantify and evaluate the variation in ABL ring distortions reported in numerous crystal structures of the Lindqvist, Keggin, and Wells–Dawson anions, histograms of these "short and long" bond lengths, $d(M-O)$, for both molybdates and tungstates were constructed from all available structures within the Cambridge Structural Database (CSD; Figure 2).[33] Two key features emerge from the analysis. First, the *averaged* $d(M-O)$ values lie within a narrow range, 1.91–1.93 Å, and are invariant to both the POM framework and metal constitution. Second, despite this fact, the tungstates and molybdates do show significant differences in the pattern of their $d(M-O)$ distributions. Polyoxotungstates have a single narrow distribution centered at ~1.92 Å, with a standard deviation less than 0.04 Å in all three frameworks. Consequently, the tungstates are best represented as nondistorted or *symmetric* structures. For molybdates, the histograms span a

(31) See, for example, a review on this subject: Poblet, J. M.; López, X.; Bo, C. *Chem. Soc. Rev.* **2003**, *32*, 297.
(32) (a) López, X.; Maestre, J. M.; Bo, C.; Poblet, J. M. *J. Am. Chem. Soc.* **2001**, *123*, 9571. (b) López, X.; Bo, C.; Sarasa, J. P.; Poblet, J. M. *Inorg. Chem.* **2003**, *42*, 2634. (c) López, X.; Poblet, J. M. *Inorg. Chem.* **2004**, *43*, 6863. (d) Maestre, J. M.; López, X.; Bo, C.; Casañ-Pastor, N.; Poblet, J. M. *J. Am. Chem. Soc.* **2001**, *123*, 3749.
(33) Allen, F. H. *Acta Crystallogr.* **2002**, *B58*, 380.

Figure 2. Histograms representing all the metal–oxygen bridging bonds for Lindqvist- (a), Keggin- (b), and Dawson-type (c) clusters (gray bars for M = W; white bars for M = Mo). All bond lengths are rounded to the nearest 0.01 Å.

wider distribution of $d(M-O)$ values, which increases with the M_nO_n ring size and may show multiple peaks depending on the structure. The shortest and longest distances observed for the molybdates are 1.81 and 2.03 Å (Lindqvist), 1.78 and 2.08 Å (Keggin), and 1.75 and 2.17 Å (Wells–Dawson). For the Keggin molybdates (Figure 2b), three peaks are distinguished within the histogram. This trimodal distribution can be decomposed into a single distribution centered at 1.92 Å, represented by more *symmetric* structures, and a bimodal distribution derived from *nonsymmetric* structures (peaks at 1.85 and 2.00 Å) that exhibit the ABL distortion pattern. Three well-defined peaks in the distribution are observed because structures with group IVA heteroatoms give histograms with only the bimodal distribution, since no undistorted structures are reported (Supporting Information, Figure S1), whereas both symmetric and nonsymmetric forms exist for anions of lower negative charge (X = P and As). This suggests that increasing the negative charge of the internalized formal XO_4^{q-} unit favors the formation of ABL distortions within the Mo_6O_6 rings. The histogram of hexamolybdate resembles that of hexatungstate but has a larger width in the apparent single $d(M-O)$ distribution. This increased width

Table 1. Experimental and Computed Average Mo–O ABL Distortions, Δd,[a] for the Edge-, Corner-, and Belt Corner-Sharing Mo–O–Mo Bridges of Lindqvist, Keggin, and Dawson Polyoxomolybdates

	Mo$_6$	PMo$_{12}$	SiMo$_{12}$	P$_2$Mo$_{18}$
Δd Mo–O$_{edge}$	0.05 (0.08)	0.11 (0.12)	0.16 (0.13)	0.19 (0.16)
Δd Mo–O$_{corner}$		0.12 (0.15)	0.17 (0.16)	0.28 (0.25)
Δd Mo–O$_{corner'}$				0.33 (0.30)
ΔE^b	−0.35	−0.8	−4.3	−8.5

[a] $\Delta d = d(\text{Mo–O})_{long} - d(\text{Mo–O})_{short}$. Average values in angstroms. Computed values in parentheses. [b] Calculated energy difference between the distorted and symmetric forms, $\Delta E = E_{dist} - E_{sym}$, in kilocalories per mole.

indicates a greater propensity for the molybdate structure to distort, although a potential bimodal distribution is masked because many of the distorted molybdate structures show a maximal distortion in only one of the three rings, thus giving more weight to the undistorted distribution. In contrast, the hexatungstate structures are undistorted within the precision of the measurements featuring quasi-O_h symmetry.[20] For the larger Wells–Dawson clusters, a more diffuse pattern is apparent in the histogram (Figure 2c). This principally reflects the presence of two different rings, Mo$_8$O$_8$ and Mo$_6$O$_6$, and to a lesser extent the three different types of bridging Mo–O bonds that derive from edge-sharing, corner-sharing, and "belt" corner-sharing oxygen atoms, where the latter link the two halves of the anion. The wider distribution may also reflect the statistics of small sampling, because only three molybdate X-ray structures (two for X = P; one for X = As) and one tungstate structure (X = P) are available within the precision constraints imposed in the analysis (see Computational Methods). A representation of the Mo$_8$O$_8$ ring distortion is given in Figure S2.

To quantify the magnitudes of the ABL distortions, we define a distortion magnitude parameter, $\Delta d_i = d(\text{Mo–O}_i)_{long} - d(\text{Mo–O}_i)_{short}$, where i denotes an edge- or corner-shared oxygen and the $d(\text{Mo–O}_i)$ values are averaged over all such bonds in the POM (Figure S3). However, *experimental* values of Δd_i for a POM are calculated as the average over all available structures in the CSD, which consequently reflect the averaged distortions in the histogram data. Next, we compare these distortion magnitudes with those calculated from geometry-optimized structures using DFT with anion solvation included (see Computational Methods). Geometries for the Lindqvist, Keggin, and Wells–Dawson anions were calculated both with and without high symmetry constraints. None of the calculated tungstate structures distort from their high symmetry configurations, in agreement with experimental evidence. However, all of the molybdates are appreciably distorted. More importantly, the distortions are not random but reproduce the systematic ABL features of the M$_n$O$_n$ rings observed in the crystal structures. Indeed, the calculated distortion magnitudes are in fair agreement with the experimental averages (Table 1). Therefore, these results demonstrate that crystal "packing effects" cannot be responsible for creating the ABL distortions because such effects are not modeled in the calculations.

Both the experimental and calculated Δd distortion parameters show increases for larger M$_n$O$_n$ ring sizes (Mo$_6$ < PMo$_{12}$ < P$_2$Mo$_{18}$) and for higher negative charges of the internalized fragments (O^{2-} < PO$_4^{3-}$ < SiO$_4^{4-}$) as shown by examining the values in Table 1 from left to right. Furthermore, the distortion stabilization energies, ΔE, measured as the energy differences between distorted and symmetric structures, also increase with larger distortions, and therefore the ΔE values

Table 2. Orbital Energies and Distortion Stabilization Energies Obtained for the COSMO-Optimized D_{3h} and D_3 X$_2$Mo$_{18}$O$_{62}^{q-}$ Compounds[c]

X	sym	energy[a]		distortions (Δd)[b]				
		ΔE	E_{HOMO}	E_{LUMO}	ΔE_{H-L}	Mo–O$_{edge}$	Mo–O$_{corner}$	Mo–O$_{corner'}$
S^{VI}	D_{3h}		−6.83	−5.24	1.59			
		−1.24						
	D_3		−6.88	−5.09	1.79	0.15	0.23	0.26
Se^{VI}	D_{3h}		−6.83	−5.23	1.60			
		−0.87						
	D_3		−6.90	−5.13	1.77	0.16	0.24	0.27
P^V	D_{3h}		−6.11	−4.78	1.33			
		−8.52						
	D_3		−6.35	−4.61	1.74	0.16	0.25	0.30
As^V	D_{3h}		−6.33	−4.82	1.51			
		−10.3						
	D_3		−6.48	−4.63	1.84	0.17	0.26	0.30
Si^{IV}	D_{3h}		−5.52	−4.35	1.17			
		−17.3						
	D_3		−5.88	−4.06	1.82	0.21	0.34	0.37
Ge^{IV}	D_{3h}		−5.65	−4.36	1.30			
		−16.8						
	D_3		−5.94	−4.05	1.89	0.22	0.35	0.39

[a] $\Delta E = E(D_3) - E(D_{3h})$ (kcal mol^{-1}); $\Delta E_{H-L} = E_{LUMO} - E_{HOMO}$ (eV). [b] $\Delta d = d(\text{Mo–O})_{long} - d(\text{Mo–O})_{short}$. Average values in angstroms. [c] Also listed are the computed average differences (Δd) between short and long bridging Mo–O distances for the edge-, corner-, and belt corner-sharing bonds in the D_3 structures.

also show the same trends. The influence of the internalized fragment charge, XO$_4^{q-}$, is investigated further in calculations on the symmetric (D_{3h}) and distorted (D_3) forms of the following series of Wells–Dawson complexes (Table 2): X$_2$M$_{18}$ (M = Mo and W; X = S^{VI}, Se^{VI}, P^V, As^V, Si^{IV}, and Ge^{IV}).[34] The tungstate structures in this series remain undistorted (data not shown), in agreement with experiment. However, the distorted chiral structures are all more stable for the molybdates. Moreover, both the distortions and stabilization energies become larger as the negative charge increases for the internal fragments, XO$_4^{q-}$, but they change much less when comparing between anions with iso-charged fragments of the third and fourth period heteroatoms, X. For example, the $\Delta d_{corner'}$ and ΔE values increase in the following order: S$_2$Mo$_{18}$ (0.26 Å; −1.24 kcal mol^{-1}) < P$_2$Mo$_{18}$ (0.30 Å; −8.52 kcal mol^{-1}) < Si$_2$Mo$_{18}$ (0.37 Å; −17.23 kcal mol^{-1}). However, the variation is much less pronounced when substituting the third period central heteroatom for its fourth period congener; for example, P$_2$Mo$_{18}$ (0.30 Å; −8.52 kcal mol^{-1}) versus As$_2$Mo$_{18}$ (0.30 Å; −10.3 kcal mol^{-1}). Therefore, it is the charge of XO$_4^{q-}$, not its size that exerts greater influence on the ABL distortions in these structures. Furthermore, the Δd values increase as the bond angles of the Mo–O–Mo units become larger. Typical Mo–O–Mo bond angles in the three structures are edge-shared bridging oxygen, ~125° (present in all three structures); corner-shared bridging oxygen, ~150° (Keggin and Wells–Dawson); and "belt" corner-shared bridging oxygen that links the two halves of the anion, ~165° (Wells–Dawson). This trend is not reflected that strongly in the Keggin complexes for which calculated Δd values are larger by only 0.03 Å for corner-shared versus edge-shared Mo–O–Mo units in PMo$_{12}$ and SiMo$_{12}$. However, within the entire X$_2$Mo$_{18}$ series, the differences are much more pronounced. In P$_2$Mo$_{18}$, the calculated Δd values for the Mo–O$_{edge}$,

(34) Si$_2$Mo$_{18}$ and Ge$_2$Mo$_{18}$ are unknown but are included to widen the scope of the analysis. Repulsion between the two internalized SiO$_4^{4-}$ or GeO$_4^{4-}$ fragments may prevent their formation of Wells–Dawson molybdate structures.
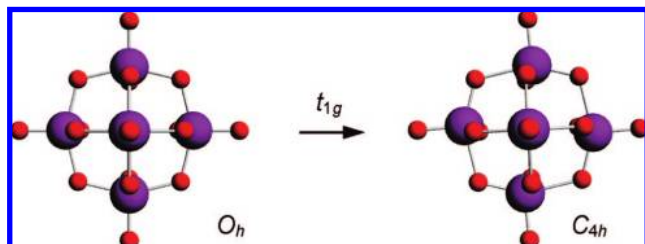
Figure 3. Nuclear motion for one component of the t_{1g}-symmetrized displacement featuring a concerted M−O ABL distortion in the M_4O_4 ring.

Figure 4. Calculated adiabatic potential energy surface along one branch of the t_{1g} mode for $[Mo_6O_{19}]^{2-}$.

Mo−O_{corner}, and "belt" Mo−O_{corner} bonds are 0.16, 0.25, and 0.30 Å respectively. Finally, an inverse correlation also exists between the magnitude of the ABL distortions and the HOMO−LUMO (H−L) gap energies of the symmetric structures. This is shown, for example, in the series X_2Mo_{18} (calcd $\Delta d_{corner'}$; ΔE_{H-L}): S_2Mo_{18} (0.26 Å; 1.59 eV), P_2Mo_{18} (0.30 Å; 1.33 eV), Si_2Mo_{18} (0.37 Å; 1.17 eV). Because the H−L gaps increase substantially on distortion for all the complexes, this suggests that the geometry change is accompanied by mixing of occupied and unoccupied frontier MOs (i.e., vibronic mixing). The detailed features of this vibronic coupling can be obtained in part from vibrational frequency calculations, which are very computationally demanding[35] for all but the smallest of POMs in this study. Consequently, we proceed here by establishing the PJT vibronic origin of the ABL distortions for the Lindqvist structure and describe the vibronic features in detail, even though it is the least distorted of the structures examined here. Then we discuss the vibronic nature of the ABL distortions in the larger POMs as well as rationalize the trends in Tables 1 and 2.

PJT Vibronic Coupling in the Lindqvist Structure Anions. In crystal structures of the molybdate and tungstate Lindqvist anions, the ABL distortions observed in any given M_4O_4 ring consist of two sets of different short (S_n) and long (L_n) M−O bonds.[15,16,20] These bond lengths alternate in the following pattern, $\{S_1-L_1-S_2-L_2\}_2$, thereby changing the local ring symmetry from undistorted D_{4h} to C_{2h}. Geometry optimizations using DFT at the BP86 level (both with and without solvent modeling; see Computational Methods) successfully reproduce this ABL pattern for Mo_6 and also predict a W_6 structure that remains undistorted from O_h symmetry. Furthermore, vibrational frequency calculations on Mo_6 using full O_h symmetry consistently show an imaginary frequency for the lowest energy vibrational mode (t_{1g}, $i81$ cm^{-1}), indicating negative curvature for the adiabatic potential energy surface along this triply degenerate symmetrized displacement coordinate.[35,36] Each branch of this mode describes concerted Mo atom off-center displacements within one of the three Mo_4O_4 rings, consistent with the gross features of the ABL distortions observed in the crystal structures (Figure 3). Consequently, the frequency calculation identifies the t_{1g} mode as a Mo_4O_4 ring ABL mode, and because the $^1A_{1g}$ electronic ground state is nondegenerate,
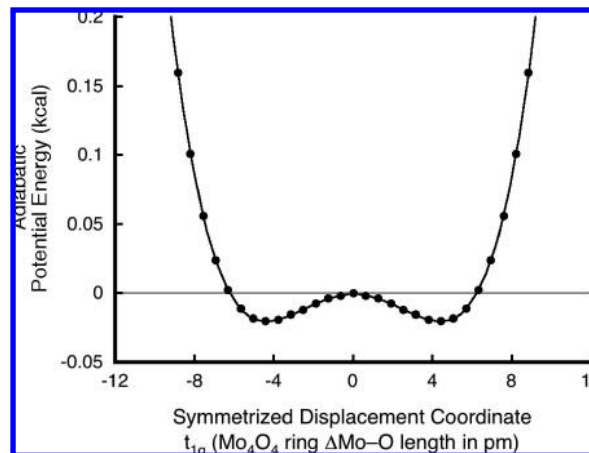
it also identifies it to be pseudo Jahn−Teller active and predicts a vibronic instability of the O_h configuration along this distortional coordinate characteristic of the strong vibronic coupling limit, $\Delta < F^2/K_0$.[37] Single-point energy calculations along the adiabatic potential energy surface of one component of the t_{1g} ABL mode confirm the characteristic feature of the vibronic instability at the O_h configuration (Figure 4). However, because this mode should have considerable anharmonic character because of both the strong vibronic coupling and the fairly large amplitudes of the metal atom displacements, the surface is considered only qualitative at best. Even so, the small PJT distortion energy, measured as the energy difference between the distorted and O_h structures, implies that the zero point energy of the distorted isomer would be above the barrier for interconversion between the two distorted minima. Therefore, the calculations suggest that the ABL distortion in Mo_6 should be considered dynamic and that the vibronic coupling condition for Mo_6 is perhaps better represented by $\Delta \approx F^2/K_0$, since the adiabatic potential energy surface is nearly flat with anticipated displacements Δd of approximately ± 8 pm at ambient temperature. However, for W_6, the calculated vibrational frequencies are all real, with the t_{1g} ABL mode frequency calculated to be 112 cm^{-1}, indicating positive curvature along its adiabatic potential energy surface, which is characteristic of the weak vibronic coupling limit, $\Delta > F^2/K_0$.[37]

Further information on the nature of the ABL distortion and the differences in vibronic coupling between Mo_6 and W_6 can be obtained from an examination of the Δ and F vibronic parameters, although F is only evaluated qualitatively here. For these Lindqvist anions, symmetry considerations on F dictate that only T_{1g} excited electronic states can mix into the $^1A_{1g}$

(35) (a) Bridgeman, A. J.; Cavigliasso, G. *Chem. Phys.* **2002**, *279*, 143. (b) Bridgeman, A. J. *Chem. Phys.* **2003**, *287*, 55.

(36) In ref,[35a] the authors used the ADF2000.02 package to numerically compute vibrational frequencies for the Lindqvist anions and commented that imaginary frequencies were produced using default settings (not identified) but disappeared using higher integration accuracy (10^{-7}) and "convergence" criteria (10^{-6}). We did not observe this behavior using ADF2006.01, where the respective default settings are 10^{-4} and 10^{-2} (gradient convergence). Increasing these to 10^{-6} and 10^{-4} maintained the imaginary frequency for the lowest t_{1g} mode.

(37) The linear vibronic mixing of two *nondegenerate* electronic states (PJT coupling) is described by three vibronic parameters: 2Δ, the energy separation between the unmixed states; F, the vibronic matrix element for mixing the two states along a symmetrized nuclear displacement coordinate, Q, where $Q_0 = 0$ is defined at the high symmetry "undistorted" nuclear configuration; and K_0, the harmonic nonvibronic force constant of the Q displacements, which for simplicity is assumed to be the same in both states. The vibronic mixing reduces the force constant along Q on the ground-state surface by an amount $K_v = F^2\Delta$, the vibronic contribution, where $K = K_0 - K_v$. Therefore, the condition $K_v > K_0$ leads to negative curvature of the adiabatic potential energy surface, and therefore a vibronic instability occurs at $Q = 0$, which defines the strong coupling limit, $\Delta < F^2/K_0$. Otherwise, K_v simply softens the adiabatic potential energy surface of the Q displacements, which defines the weak coupling limit, $\Delta > F^2/K_0$. See ref[5c] for further details.
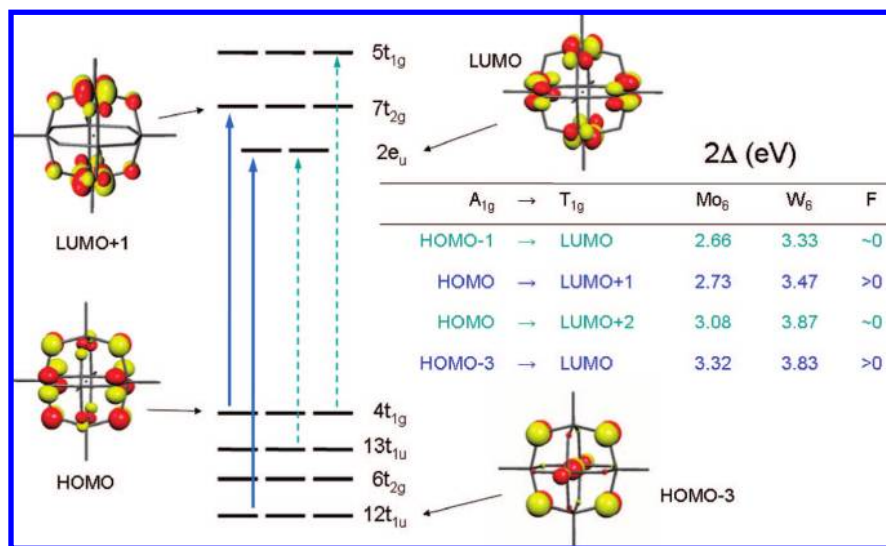
Figure 5. Frontier orbital diagram for $[Mo_6O_{19}]^{2-}$ showing the principal orbital excitations associated with the four lowest energy $A_{1g} \rightarrow T_{1g}$ electronic (radiationless) transitions. The T_{1g} excited-state energies (2Δ) obtained from time-dependent DFT calculations and the sign of the vibronic parameter F are also shown for both $[Mo_6O_{19}]^{2-}$ and $[W_6O_{19}]^{2-}$. Solid blue arrows represent the transitions contributing significantly in the PJT coupling (see text).

ground state by the PJT-active t_{1g}-symmetrized nuclear displacements identified from the frequency calculations. Using time-dependent DFT methods,[38] we calculated the energies (2Δ) of the four lowest energy T_{1g} excited states of Mo_6 and W_6 (Figure 5). The orbital configurations of these states indicate substantial $O \rightarrow M$ charge transfer character (Figures 5 and S4). However, only two of these excited states, those represented by the orbital excitations t_{1g} (HOMO) $\rightarrow t_{2g}$ (LUMO + 1) and t_{1u} (HOMO − 3) $\rightarrow e_u$ (LUMO) from the ground-state configuration, contribute significantly to the PJT coupling ($F > 0$, Figure 5). The other two T_{1g} states, represented by the orbital excitations, t_{1u} (HOMO − 1) $\rightarrow e_u$ (LUMO) and t_{1g} (HOMO) $\rightarrow t_{1g}$ (LUMO + 2), have poor overlap under the influence of the t_{1g} ABL mode ($F \approx 0$, Figure S4). Further examination of the two important orbital vibronic contributions shows that the excitation $t_{1g} \rightarrow t_{2g}$ leads to a short−long $O-M-O$ ABL pair for only two metal centers that are located on opposite sides of the M_4O_4 ring, whereas for $t_{1u} \rightarrow e_u$, the short−long bond alternation persists equally throughout the ring (Figure 5). On combination, these two contributions account for the experimentally observed $\{S_1-L_1-S_2-L_2\}_2$ ABL distortion pattern, which stems from vibronic-induced increases in O_p-M_d π-covalency and associated $O \rightarrow M$ charge transfer from otherwise nonbonding metal and oxygen orbitals. Furthermore, the vibronic analysis shows that the larger ABL ring distortions observed in Mo_6 relative to those of W_6 derive in part from electronegativity considerations on the vibronic coupling parameters. A smaller K_v[37,39] value for W_6 originates from larger Δ and smaller F vibronic parameters, which are both related to the lower electronegativity of tungsten relative to that of molybdenum. A smaller F value for W_6 is not proven here but is anticipated from electronegativity-related decreases in $O \rightarrow M$ charge transfer and poorer O_p-M_d π-orbital overlap considerations for tungsten.

PJT Vibronic Coupling in Keggin and Wells−Dawson Molybdates and the Influence of "Crystal Packing Effects". The PJT vibronic interaction in Mo_6 does not involve direct HOMO−LUMO mixing, although the H−L gap does widen from 2.55 eV (O_h) to 2.63 eV (S_6) because of mixing with other frontier orbitals. For POMs in general, the compositions of the frontier MOs exhibit little variation, being essentially of nonbonding O_p-type (occupied) and M_{dxy}-type (unoccupied) character as in Mo_6 (Figure 5).[31,32] Because of this similarity, and the fact that the H−L gaps all widen for the Keggin and Wells−Dawson molybdates on distortion to their chiral ABL structures (Table 2), the origin of the ABL distortions observed in these and other POMs is expected to be the same as that in Mo_6 (i.e., PJT vibronic coupling). Furthermore, although detailed knowledge of the number of coupled excited states and associated excitation energies, Δ_i, is not known at this time for the other POMs examined here, the H−L gap energy approximates the average of the excitation energies for excited states involving the H−L orbitals. Therefore, the H−L gap is a reasonable substitute for 2Δ in a qualitative vibronic analysis of these anions.

As noted earlier, increases in both the distortion stabilization energies, ΔE, and the extent of distortions, Δd, within a series of Lindqvist, Keggin, and Wells−Dawson molybdates correlate with (1) larger Mo_nO_n ring sizes, (2) higher charges of internalized fragments, and (3) smaller H−L gaps for the symmetric structures (Tables 1 and 2). Furthermore, larger molybdenum displacements are observed within $Mo-O-Mo$ fragments that have larger bond angles. Finally, a bimodal distribution in the experimental $d(Mo-O)$ values, shown in histograms for a given POM structure (Figure S1), crosses over toward a trimodal or a single broad distribution (Figure 2) as the computed distortion stabilization energies become smaller.

These observations can be explained by the following arguments. First, the connection between molybdenum atom displacements and the POM size (Table 1) is traced to differences in H−L gap energies at the symmetric configurations. As the number of metal and oxygen atoms increases, larger M_nO_n rings are formed, and both the number and density of frontier MOs increase, which leads to a concomitant reduction

(38) (a) Runge, E.; Gross, E. K. U. *Phys. Rev. Lett.* **1984**, *52*, 997. (b) Casida, M. E. *Recent Advances in Density-Functional Methods*, World-Scientific: Singapore, 1995; p 155. (c) van Gisbergen, S. J. A.; Groeneveld, J. A.; Rosa, A.; Snijders, J. G.; Baerends, E. J. *J. Phys. Chem. A* **1999**, *103*, 6835.

(39) A smaller K_0 for Mo_6 relative to that of W_6 could also contribute to greater vibronic interaction observed in Mo_6, but we have no information on this quantity.

Scheme 1. Relationship between the Extent of the Pseudo Jahn−Teller Effect and the Size of the Mo_mO_{3m} Cage, Quantified through the HOMO−LUMO Gap Opening upon Distortion[a]
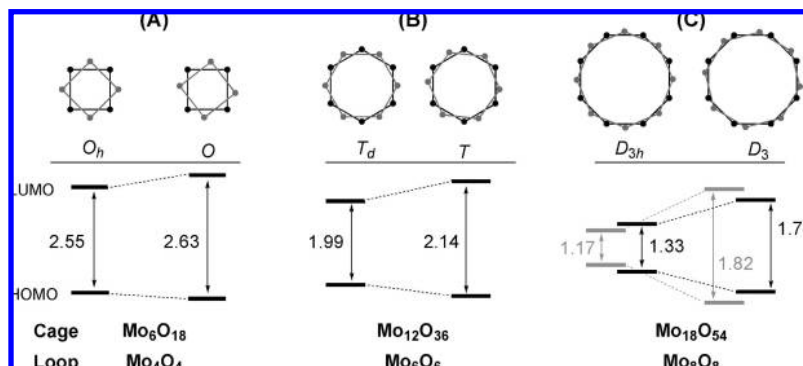
[a] The symmetric and distorted forms of the Mo_nO_n loops (n = 4, 6, 8) are depicted as black and gray rings of Mo and O. Cases: (A) $[Mo_6O_{19}]^{2-}$, (B) α-$[PMo_{12}O_{40}]^{3-}$, and (C) α-$[P_2Mo_{18}O_{62}]^{6-}$ and the hypothetical α-$[Si_2Mo_{18}O_{62}]^{8-}$ (gray font). Values are in electronvolts.

of the H−L gap at the undistorted nuclear configurations (Scheme 1).[40] Smaller H−L gaps enable greater vibronic mixing between the occupied and unoccupied frontier MOs, which is detected by a widening of the H−L gaps on distortion with concomitant increases in ABL distortion magnitudes. Second, the correlation between Δd and Mo−O−Mo bond angles derives in part from expectations of a larger F vibronic parameter. Bond angles approaching 180° should increase F by facilitating greater M_d−O_p π-overlap. The correlation is particularly striking within the X_2Mo_{18} series (Table 2). Third, with respect to the influence of the internalized fragment charge on the ABL distortions, further insight can be gained by examining a "clathrate" model[41] of the Wells−Dawson P_2M_{18} structure. This model consists of a neutral $M_{18}O_{54}$ framework that encapsulates two PO_4^{3-} fragments. In the absence of the internal phosphate anions, our calculations show that the hypothetical neutral $M_{18}O_{54}$ cage would adopt a nondistorted D_{3h} structure for M = W and Mo. Next, we calculated the energy of the $M_{18}O_{54}$ cage after inclusion of both phosphate anions with geometry optimization constrained to D_{3h} symmetry (Figure S5). The presence of the two anions induces a significant electronic and geometric reorganization of the $M_{18}O_{54}$ cage that requires similar energies for the molybdate (123 kcal mol^{-1}) and tungstate (130 kcal mol^{-1}) cages. The deformation of the $M_{18}O_{54}$ moiety from the symmetric form to the distorted geometry is also endothermic, but the energy is relatively small for M = Mo (12.9 kcal mol^{-1}) and significantly larger for M = W (36.3 kcal mol^{-1}). The latter value was estimated by assuming the distorted molybdate geometry for the P_2W_{18} calculation. Moreover, other computational investigations have shown that increasing the charge of the internal fragment within a POM raises the energy of the occupied and unoccupied molecular orbitals, with the effect being more pronounced for oxygen than that for metal orbitals.[42] This effect also is demonstrated herein for the X_2Mo_{18} series from examination of the H−L energies (Table 2). Consequently, the H−L energy gap decreases as the internal fragment charge increases, which favors distortion as described earlier.

Finally, we discuss the connection between the computed distortion stabilization energy of a POM (Tables 1 and 2) and the variations observed in its experimental d(M−O) bond lengths (Figure 2). The calculated ΔE values for Mo_6 and PMo_{12} are

only −0.35 and −0.8 kcal mol^{-1}, respectively. Furthermore, the fairly flat adiabatic potential energy surface along the ABL distortion mode for Mo_6 indicates that the PJT vibronic distortion is dynamic over a wide range of d(Mo−O) values ($\sim\pm0.08$ Å), which suggests that Mo_6 is in the intermediate to strong vibronic coupling limit. The same is likely true for both PMo_{12} and S_2Mo_{18} based on their small ΔE values. Molecular systems with vibronic coupling in this regime often show large variability in vibronic-induced distortions as observed across multiple crystal structures of the same molecule.[43] In such cases, the influence of the lattice parameters (i.e., "packing effects"), including the nature of the counterions, space group symmetry, temperature, strain, solvent of crystallization, and so forth, can impact on both the magnitude and dynamics of the vibronic distortions by reshaping the adiabatic potential energy surface for the motion. These "packing effects" either amplify or diminish the vibronically induced distortion but do not cause it. The origin of the distortion lies in the vibronic-induced softening of the force constant along the distortional coordinate. Large structural variations originating from a confluence of intermediate/strong vibronic coupling with external perturbations are not uncommon and have been described as a "plasticity effect".[43] The histograms representing d(Mo−O$_i$) bond lengths from the many crystal structures of Mo_6 and PMo_{12} are consistent with this behavior. The calculated Δd_i values for these two anions (0.08 Å for Mo_6; 0.12 and 0.15 Å for PMo_{12}) overestimate the *averaged* experimental values (0.05 Å for Mo_6; 0.11 and 0.12 Å for PMo_{12}) because of averaging over both symmetric and distorted experimental structures, which lowers the averaged experimental Δd_i values. Near the edges of the d(W−O) distributions for the W_6 and XW_{12} structures, a few show significant ABL distortions having Δd values of ~0.07 and ~0.11 Å, respectively. These complexes are in the weak vibronic coupling limit in the absence of crystal packing forces, but presumably the ABL mode is sufficiently softened (frequency calculated to be 112 cm^{-1} for W_6) such that suitable crystal fields can amplify the vibronic distortions somewhat. Precise mechanistic details of the lattice conditions necessary for this amplification are unknown at this time but are under investigation. For POMs with sufficiently large ΔE values, a predominance toward distorted structures is expected with less variation in d(M−O$_i$) values. Indeed, several structural reports on $SiMo_{12}$ (calculated ΔE = −4.3 kcal mol^{-1}) show only large

(40) López, X.; Fernández, J. A.; Poblet, J. M. *Dalton Trans.* **2006**, 1162.

(41) Day, V. W.; Klemperer, W. G. *Science* **1985**, *228*, 533.

(42) López, X.; Fernández, J. A.; Romo, S.; Paul, J. F.; Kazansky, L.; Poblet, J. M. *J. Comput. Chem.* **2004**, *25*, 1542.

(43) For a recent review, see: Murphy, B.; Hathaway, B. *Coord. Chem. Rev.* **2003**, *243*, 237, and references therein.

ABL distortions in contrast to the lower charged Mo_6 and PMo_{12} anions (Figure S1).

Vibronic Distortions in Tungstates. Of the polyoxotungstates examined herein, only the crystal structures of P_5W_{30} consistently show statistically significant ABL ring distortions. The distortions occur within the two $W_{10}O_{10}$ rings (Figure S2) with shortest and longest experimental $d(W-O)$ bond lengths of 1.80 and 2.09 Å and mean values of 1.82 and 2.06 Å, respectively.[23] Some of us recently reported a computational investigation on the undistorted D_{5h} symmetry structure of P_5W_{30}.[40,44] We report here that the experimental ABL distortions are reproduced reasonably well in a geometry optimization calculation by relaxing the symmetry constraints to D_5, giving 1.83 and 2.14 Å for the shortest and longest W−O bond lengths. The calculated H−L gap energy in the undistorted anion is 2.09 eV.[45] This is similar to the computed gaps for the Keggin molybdates, but smaller than those in the W_6-W_{18} clusters, which typically show values approximately 0.7−0.8 eV larger than those for the homologous molybdates.[18b,27] With respect to the undistorted form of P_5W_{30}, the chiral distorted structure is calculated to be 10.5 kcal mol^{-1} lower in energy and the H−L gap of 2.31 eV is substantially larger, which, as in the molybdates, is consistent with a PJT vibronic instability of the high symmetry configuration. This instability, as well as its absence in the other tungstates examined here, derives from a combination of the larger ring size and associated smaller H−L gap in P_5W_{30}.

Structural Distortions in Reduced Mixed-Valence POMs. The addition of electrons to the formally d^0 metal oxide structures of POMs usually results in class II mixed-valence behavior according to the Robin and Day classification scheme.[46,47] We now consider how this mixed-valence electronic structure influences the ABL ring distortions within α-Wells−Dawson anions. Neier et al. report crystal structures on both the oxidized and two-electron reduced forms of PMo_{12} and S_2Mo_{18}, which show significantly smaller ABL distortions in the reduced anions.[17c] In S_2Mo_{18}, the averaged long and short bonds change from 2.04 and 1.79 Å in the oxidized complex to 1.95 and 1.88 Å upon reduction. Our DFT calculations on both oxidized and one-electron reduced X_2Mo_{18} systems (X = S, P, and Si)[34] show similar behavior. Indeed, both the calculated ABL distortion magnitudes (Δd) and stabilization energies (ΔE) are substantially smaller in the reduced forms. The ΔE values for the reduced complexes decrease by approximately 3, 4, and 6 kcal mol^{-1} for X = S, P, and Si, relative to the oxidized species (Figure 6). Whereas increasing the anion charge by XO_4^{q-} substitution enhances the ABL distortion, this result shows that POM reduction has the opposite effect, since the added electrons populate metal−oxygen π-antibonding orbitals, reducing the ABL distortion. Consequently, DFT calculations predict that a less distorted structure would be energetically more favorable for mixed-valence POMs relative to their fully oxidized forms.
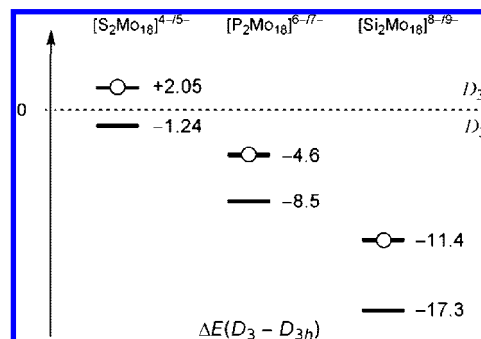
Figure 6. Effect of increasing the anion charge (XO_4^{q-} versus one-electron reduction) on the calculated distortion stabilization energies, ΔE (kcal mol^{-1}), of α-$[X_2Mo_{18}O_{62}]^{q-}$ (X = S, P, and Si): oxidized form (lines); one-electron reduced (circles and lines).

The "anomalous" electrochemical behavior of P_2Mo_{18} was the first chemical property attributed to ABL distortions in a POM.[25] Polarograms of this anion in aqueous solution feature several indivisible two-electron reduction steps[28a,29a] in contrast to the corresponding tungstate, P_2W_{18}, which shows multiple one-electron processes under the same conditions.[29b] Pope and Garvey proposed that the chiral ABL distortion in P_2Mo_{18} cathodically shifts the first one-electron reduction sufficiently that it becomes superimposed onto the second reduction feature.[25] From an analysis of available POM redox potentials,[28,29,48] these investigators estimated the cathodic shift to be 0.17 V. We note that the proposed superposition is consistent with the approximately 0.2 V separations observed between successive one-electron reduction potentials in aqueous solutions of undistorted POMs.[28,29,48] However, the influence of the chiral ABL distortion on the redox behavior of P_2Mo_{18} has been questioned[49a] because of the appearance of separate monoelectronic reductions, spaced apart by approximately 0.13 V, in cyclic voltammograms of the tetra-*n*-butylammonium salt of P_2Mo_{18} in acetonitrile.[49] In our view, however, this redox behavior is entirely consistent with Garvey and Pope's proposal. The differences between the first and second one-electron reduction potentials increase to 0.4−0.5 V for undistorted POMs in acetonitrile solution (using tetra-*n*-butylammonium salts to minimize potential ion-pairing effects),[50] which is sufficiently large to enable separation of these redox processes in P_2Mo_{18}. Furthermore, this separation, being only 0.13 V, is significantly smaller than that in undistorted POMs, which again is consistent with the proposed vibronic-induced cathodic shift of the first reduction potential. Indeed, using the same approach as Garvey and Pope for estimating the cathodic shift in aqueous solutions,[25] we note that the difference between the first one-electron reduction potentials in tetra-*n*-butylammonium salts of P_2W_{18} (−0.847 V) and P_2Mo_{18} (−0.60 V)[49] in acetonitrile is 0.25 V, whereas the difference between those of PW_{12} (−0.601 V)[49a] and PMo_{12} (−0.170 V)[49a] is 0.43 V. This suggests a 0.18 V vibronic-induced cathodic shift in the first reduction potential of P_2Mo_{18} in acetonitrile, which is nearly identical to that estimated by Garvey and Pope for P_2Mo_{18} in water. Our DFT calculations also support Garvey and Pope's hypothesis. Using

(44) Fernández, J. A.; López, X.; Bo, C.; de Graaf, C.; Baerends, E. J.; Poblet, J. M. *J. Am. Chem. Soc.* **2007**, *129*, 12244.

(45) This value does not fully agree with the latest calculations reported by our group on the same system (ref). The reason is that, in the present article, we report the full COSMO-optimized Preyssler structure, whereas in the past the geometry was optimized in the gas phase followed by a single point run in COSMO.

(46) (a) Sanchez, C.; Livage, J.; Launay, J. P.; Fournier, M.; Jeannin, Y. *J. Am. Chem. Soc.* **1982**, *104*, 3194. (b) Sanchez, C.; Livage, J.; Launay, J. P.; Fournier, M. *J. Am. Chem. Soc.* **1983**, *105*, 6817. (c) Suaud, N.; Gaita-Ariño, A.; Clemente-Juan, J. M.; Sánchez-Marı´n, J.; Coronado, E. *J. Am. Chem. Soc.* **2002**, *124*, 15134, and references therein.

(47) Robin, M.; Day, P. *Adv. Inorg. Chem. Radiochem.* **1967**, *10*, 247.

(48) Fruchart, J. M.; Hervé, G.; Launay, J. P.; Massart, R. *J. Inorg. Nucl. Chem.* **1976**, *38*, 1627.

(49) (a) Himeno, S.; Maeda, K.; Osakai, T.; Saito, A.; Hori, T. *Bull. Chem. Soc. Jpn.* **1993**, *66*, 109. (b) Barrows, J. N.; Pope, M. T. *Inorg. Chim. Acta* **1993**, *213*, 91.

(50) Maeda, K.; Katano, H.; Osakai, T.; Himeno, S.; Saito, A. *J. Electroanal. Chem.* **1995**, *389*, 167.

an approach that successfully reproduces experimentally measured reduction potential differences between POMs,[40,51] we calculate the cathodic shift from the difference in electron affinity between the D_{3h} and D_3 forms of P_2Mo_{18} via their LUMO energies (Table 2). The cathodic shift is calculated to be 0.17 V, in good agreement with the 0.18 V shift estimated from experiment. In the smaller polyoxomolybdates, Mo_6 and XMo_{12}, separate one-electron reduction processes are observed because the PJT vibronic interactions are much weaker relative to those of P_2Mo_{18}.

Conclusions

A systematic search in a structural database allows us to evaluate the extent of alternating bond length distortions and related chirality in well-known polyoxomolybdates and polyoxotungstates. DFT calculations show that these metal oxide ring distortions originate from a pseudo Jahn−Teller vibronic instability at high symmetry configurations. For the smallest polyoxomolybdate, $[Mo_6O_{19}]^{2-}$, a vibrational analysis at O_h symmetry identifies an imaginary frequency for an alternating bond length distortion mode (t_{1g}, $i81$ cm^{-1}), which implies negative curvature of the adiabatic potential energy surface and therefore a pseudo Jahn−Teller vibronic instability along this mode at the O_h configuration. The nuclear distortion transforms formally nonbonding occupied oxo and unoccupied metal frontier orbitals into Mo−O π-bonding and π*-antibonding orbitals that lead to a concerted bond alternation within the Mo_4O_4 rings. Only two orbital vibronic couplings contribute significantly to the distortion and are sufficient to model the $\{(short-long)_1-(short-long)_2\}_2$ Mo−O bond length alternation pattern observed in the crystal structures. Calculations on other polyoxometalate structures also are consistent with a pseudo Jahn−Teller vibronic origin for the alternating bond length distortions in these systems and enable the following conclusions: (1) greater ring distortions are observed in larger polyoxometalates because of decreased HOMO−LUMO gaps, (2) increasing the negative charge of fragments (O^{2-} or XO_4^{q-}) incorporated within the Mo_mO_{3m} cages favors distortion because of decreased HOMO−LUMO gaps, (3) increased charge by adding electrons to the structures has the opposite effect (i.e., it inhibits bond alternation by populating metal−oxygen π*-antibonding orbitals that destabilize the distorted form, thus favoring structures of higher symmetry), (4) the vibronic distortion can be detected in sufficiently distorted oxidized POMs by a decreased separation in their first and second reduction potentials, as shown for P_2Mo_{18}, and (5) distortions in tungstates are not as common as those in molybdates because their HOMO−LUMO gaps are substantially larger. Even so, our calculations show that the Preyssler anion (a W_{30}-based cluster) is large enough such that the HOMO−LUMO gap closes sufficiently to form a vibronic alternating bond length distortion.

Computational Methods

All calculations were performed by using the density functional-based ADF2004.01 package.[52] Equilibrium structures and associated

energies were obtained at the BP86 level within the framework of the generalized gradient approximation, applying the $X\alpha$ model with Becke's corrections[53] for describing exchange, and the VWN parametrization[54] with Perdew's corrections[55] for correlation. We optimized all the geometries by using the conductor-like screening model (COSMO)[56] to account for solvent effects (CH_3CN, $\varepsilon =$ 36.74). The choice of this specific dielectric constant is of limited importance in the present analysis and, moreover, corresponds to the common use of CH_3CN in electrochemical studies of Dawson polyoxomolybdates.[57] To describe the valence electrons, we used a Slater-TZP-quality basis set. The core electrons (O: 1s; Na, Si, P, S: 1s−2p; Mo: 1s−3d; W: 1s−4d) were kept frozen and described by single Slater functions. We applied scalar relativistic corrections to them via the zeroth-order regular approximation with the core potentials generated using the DIRAC program.[52] The solvent cavity surrounding the anions was created using the solvent-excluding method with fine tesserae. The ionic radii for the atoms which actually define the size of the solvent cavity were chosen to be 1.26 and 1.52 for W^{6+} and O^{2-}, respectively. We applied the spin-unrestricted formalism to open-shell species.

Geometry optimizations were carried out with symmetry constraints. For the undistorted idealized Lindqvist, Keggin, Dawson, and Preyssler clusters, their real maximal symmetries (O_h, T_d, D_{3h}, and D_{5h}, respectively) were used. For the distorted cases, in which not all the symmetry point groups are available in the ADF package, C_i (instead of the formally ideal S_6), C_1 (instead of T), D_3, and D_5 point groups were employed, respectively.

For the vibronic analysis on Mo_6 and W_6, the ADF2006.01 package was used for all computations using the same basis sets and implementation of COSMO as described earlier. Two-point numerical frequency calculations were performed with an integration accuracy of 5.5 and gradient convergence of 3.0 above the default values of 4.0 and 2.0, respectively. This approach eliminates all odd-order anharmonic force constant terms. Analytical frequency calculations with an integration accuracy of 6.0 gave similar results, including the imaginary frequency for the lowest energy t_{1g} mode. The adiabatic potential energy surface was calculated along the t_{1g} displacement coordinates (obtained from the frequency calculation) with an integration accuracy of 8.0 using TZP (Mo; 1s−3d frozen) and TZ2P (O; all electron) basis sets. The time-dependent DFT calculations were performed with the same basis set for oxygen but used an all-electron TZP basis set for Mo in addition to the gradient-regulated asymptotic correction potential.[58] The lowest energy dipole-allowed electronic transition in $[Mo_6O_{19}]^{2-}$, $^1T_{1u} \leftarrow$ $^1A_{1g}$, was calculated to be 320 nm, in good agreement with the experimental maximum wavelength of absorption of 325 nm.

Database Search. The collection of structural data was obtained through a systematic search of the CSD[20] (version 5.28) for compounds of the general formulas $M_6O_{19}^{2-}$ (Lindqvist), $XM_{12}O_{40}^{q-}$ (Keggin), and $X_2M_{18}O_{62}^{q-}$ (Dawson) (M = W, Mo; X = Al, Si, Ge, P, As, S, Se). Search refinements were employed to focus on the most reliable crystal structures. These refinements excluded disordered structures or reports with errors, and the *R* value cutoff was less than 10%. The metal−oxygen bond lengths

(51) Duhacek, J. C.; Duncan, D. C. *Inorg. Chem.* **2007**, *46*, 7253.
(52) (a) *ADF2004.01*; Vrije Universiteit: Amsterdam, 2004. (b) Baerends, E. J.; Ellis, D. E.; Ros, P. *Chem. Phys.* **1973**, *2*, 41. (c) Versluis, L.; Ziegler, T. *J. Chem. Phys.* **1988**, *88*, 322. (d) Te Velde, G.; Baerends, E. J. *J. Comput. Phys.* **1992**, *99*, 84. (e) Fonseca Guerra, C.; Snijders, J. G.; Te Velde, G.; Baerends, E. J. *Theor. Chem. Acc.* **1998**, *99*, 391. (f) Te Velde, G.; Bickelhaupt, F. M.; van Gisbergen, S. J. A.; Fonseca Guerra, C.; Baerends, E. J.; Snijders, J. G.; Ziegler, T. *J. Comput. Chem.* **2001**, *22*, 931.

(53) (a) Becke, A. D. *J. Chem. Phys.* **1986**, *84*, 4524. (b) Becke, A. D. *Phys. Rev.* **1988**, *A38*, 3098.
(54) Vosko, S. H.; Wilk, L.; Nusair, M. *Can. J. Phys.* **1980**, *58*, 1200.
(55) (a) Perdew, J. P. *Phys. Rev.* **1986**, *B33*, 8822. (b) Perdew, J. P. *Phys. Rev.* **1986**, *B34*, 7406.
(56) (a) Klamt, A.; Schüürmann, G. *J. Chem. Soc., Perkin Trans. 2* **1993**, 799. (b) Andzelm, J.; Kölmel, C.; Klamt, A. *J. Chem. Phys.* **1995**, *103*, 9312. (c) Klamt, A. *J. Chem. Phys.* **1995**, *99*, 2224. (d) Model implemented in the ADF package by: Pye, C. C.; Ziegler, T. *Theor. Chem. Acc.* **1999**, *101*, 396.
(57) (a) Way, D. M.; Cooper, J. B.; Sadek, M.; Vu, T.; Mahon, P. J.; Bond, A. M.; Brownlee, R. T. C.; Wedd, A. G. *Inorg. Chem.* **1997**, *36*, 4227. (b) Zhang, J.; Bond, A. M.; MacFarlane, D. R.; Forsyth, S. A.; Pringle, J. M.; Mariotti, A. W.; Glowinski, A. F.; Wedd, A. G. *Inorg. Chem.* **2005**, *44*, 5123.
(58) Grüning, M.; Gritsenko, O. V.; van Gisbergen, S. J. A.; Baerends, E. J. *J. Chem. Phys.* **2001**, *114*, 652.

for building the histograms were obtained as those defined for all the bridging M−O bonds, using random hits as diagrammatic queries in the program ConQuest (version 1.9). The search (updated through Aug 2007) produced, for $M_6O_{19}^{2-}$ clusters, 34 and 45 hits for M = W and Mo, respectively, 12 (M = W) and 33 (M = Mo) hits for $XM_{12}O_{40}^{q-}$, and 1 (M = W) and 2 (M = Mo) hits for $X_2M_{18}O_{62}^{q-}$. For identical molecules (same counterions), we only considered the best quality X-ray structure. Additional diagrammatic queries (Figure S2) were used to distinguish between the different types of M−O−M bridging bonds in quantifying the distortion (Δd). The search (updated through Jan 2007) produced 23 hits for $PMo_{12}O_{40}^{3-}$, 7 hits for $PMo_{12}O_{40}^{3-}$, and 1 hit for $P_2Mo_{18}O_{62}^{6-}$.

Electrochemical Measurements. A cyclic voltammogram of the tetra-*n*-butylammonium salt of α-$[P_2W_{18}O_{62}]^{6-}$ was recorded using a combined potentiostat/galvanostat (PARSTAT 2273) in a three-electrode configuration with the following experimental protocols: glassy carbon working, Pt wire auxiliary, and Ag/0.01 M AgNO$_3$ reference electrodes (Bioanalytical Systems); 1 mM POM in acetonitrile with 0.1 M tetra-*n*-butylammonium hexafluorophosphate was used as supporting electrolyte and maintained at 25 °C. The measured half-wave potential, $E_{1/2} = -0.847$ V, was reported as the difference between the anodic and cathodic peak potentials. The measured ferrocene/ferrocenium redox couple (+0.090 V) under these conditions was identical to that reported in reference.[50]

Supporting Information Available: Histograms representing all of the metal−oxygen bridging bonds for Keggin anions, representations of Mo_8O_8 and $W_{10}O_{10}$ ring distortions in Wells−Dawson and Preyssler anions, structural motifs used in the CSD search, M_6 anion orbital representations of two low-lying T_{1g} excited states that mix poorly into the A_{1g} ground state by the t_{1g} vibrational mode, and $M_{18}O_{54}$ (M = Mo, W) deformation energies. This material is available free of charge via the Internet at http://pubs.acs.org.

JA711008N